journal of the mechanical behavior of biomedical materials 124 (2021) 104858

Contents lists available at ScienceDirect

Journal of the Mechanical Behavior of Biomedical Materials

journal homepage: www.elsevier.com/locate/jmbbm

Research Paper

In-silico design and experimental validation of TiNbTaZrMoSn to assess accuracy of mechanical and biocompatibility predictive models

C. Torres-Sanchez [a,*], E. Alabort [b], J. Wang [a], M. Norrito [a], P.P. Conway [a]

[a] Wolfson School of Mechanical, Electrical and Manufacturing Engineering, Loughborough University, LE11 3PE, UK
[b] Alloyed Ltd, Unit 15, Oxford Industrial Park, Yarnton, OX5 1QU, UK

ARTICLE INFO

Keywords:
Titanium
Beta alloys
TiNbTaZrMoSn
Numerical design
Surface characterisation
MC3T3-E1

ABSTRACT

Numerical design of TiNbTaZrMoSn alloy preceded its manufacture and mechanical, physico-chemical and in vitro characterisation. The specifications of the alloy required a multi-objective optimisation including lower modulus of elasticity than c.p.Ti, high strength, stabilised β crystal structure with a low martensitic start temperature, a narrow solidification range and high biocompatibility. The results reveal that there was a good match between the bulk mechanical properties exhibited by the alloy experimentally and those predicted. Regarding surface properties, independent of roughness effects, the oxide thickness and surface zeta-potential, measured in biologically relevant electrolytes and at physiological pH, arose as important factors in osteoblastic activity (i.e., cell proliferation, measured via DNA, protein and metabolite content, and differentiation, via ALP levels), but not in cell adhesion and viability. The thinner oxide layer and lower absolute value of surface zeta-potential on the TiNbTaZrMoSn alloy explain its lesser osteogenic properties (i.e., inhibition of ALP activity) compared to the c.p. Ti. This study demonstrates that the numerical models to predict microstructure and bulk mechanical properties of β-Ti alloys are robust, but that the prediction of cellular bioactivity lags behind and still requires parameterisation to account for features such as oxide layer composition and thickness, electro-chemical properties and surface charge, and topography to optimise cell response in silico before committing to the costly manufacture and deployment of these alloys in regenerative medicine.

1. Introduction

The search for alloys that fulfil the needs and specifications for biomedical applications has been steered away from reportedly toxic and physiologically harmful elements such as V, Al, Ni, and expanded towards the study of β-stabilising elements (i.e., Nb, Mo, Ta, etc) (Guo et al., 2013; Ion et al., 2014; Neacsu et al., 2015). Such elements, when alloyed with Ti, lower its stiffness and increase its ductility, mimicking the mechanical properties of bone and therefore mitigating episodes of aseptic loosening of implants in-service and stress-shielding of the host issue which arrest the natural healing process. Even small additions of these elements under cytotoxic levels are sufficient to obtain the sought-after features of Ti alloys such as manufacturability, corrosion and wearing resistance, inertness, sterilizability and good contrast during imaging procedures (e.g. tomography or magnetic resonance) (Zhang and Chen, 2019).

Much work has been undertaken with regards to the modelling and prediction of mechanical properties of Ti alloys from a numerical and computational viewpoint (Raabe et al., 2007; Huang et al., 2016; Morinaga et al., 1986; Gutiérrez Moreno et al., 2017; Datta et al., 2016). However, bulk properties are not sufficient to foresee the biological performance of a material used in an implantable medical device. Since the first interface the cells of a host tissue (e.g. bone) are exposed to is the implant surface, the outermost layer of the material deserves analysis and characterisation from both a physical and chemical viewpoint. The passivating oxide layer that spontaneously occurs in pure titanium is the main reason for its inertness, and when alloying elements are added, this layer might differ and therefore requires consideration to assess its thickness and chemical composition (Torres-Sanchez et al., 2020). While Ti is its main constituent, the addition of alloying elements can also modify the alloy's osteoconductive and osteoinductive properties (Neacsu et al., 2015; Torres-Sanchez et al., 2020; Torres-Sánchez et al., 2020; Song et al., 2014), and therefore the implant's fate in the long term since the material's properties can instruct the attachment of cells, their proliferation, differentiation, maturation and ultimately mineralisation. When β-stabilising elements are alloyed with Ti, it is appropriate

* Corresponding author.
E-mail address: c.torres@lboro.ac.uk (C. Torres-Sanchez).

https://doi.org/10.1016/j.jmbbm.2021.104858
Received 21 January 2021; Received in revised form 14 September 2021; Accepted 21 September 2021
Available online 25 September 2021

to determine if any martensitic transformation takes place, as this could jeopardise the mechanical performance of the implant if this temperature was too close or around physiological temperatures.

Attempts to predict the biocompatibility of a material in-silico have been made (Sultana et al., 2014; Kuroda et al., 1998) but this has not achieved comprehensive results since the osteogenic behaviour of cell lines are highly dependent on many external conditions that, to date, can only be truly and reliably determined ex-silico (NooriBanu and Devaki Rani, 2018).

This study reports a comprehensive study comprising design, selection, manufacture and physico-chemical, mechanical and biological characterisation of a β-type Ti alloy created with the purpose of exhibiting desirable bio-mechanical characteristics to become an implantable material for load-bearing orthopaedic applications. The design and selection of the target alloy was achieved using numerical approaches and computational multiobjective optimisation aiming low stiffness (via a metastable β alloy at room temperature), high strength, and with high levels of predicted biocompatibility, using the modelling methods currently available. Subsequently, the alloy was manufactured and characterised considering bulk and surface physico-chemical properties, and osteogenic properties were assessed to validate and determine robustness of the numerical models in the prediction of the target alloy multi-properties. The alloy performance was benchmarked against c.p. Ti, the 'gold standard' in orthopaedic implantable devices.

2. Numerical approach: alloy specification, design, selection and predicted performance

2.1. Modulus of elasticity and constituent phases

In titanium alloys, the elastic modulus and other mechanical properties change with the type of phases present in the alloy. For example, the ω-phase displays the highest elastic modulus, followed by the martensite α''-phase, thence α'-phase, while the BCC β-phase exhibits the lowest modulus (Abdel-Hady et al., 2006). The modulus is a function of the structure of the crystal, but it is also affected by the interatomic distances in the lattice. This means that one can obtain low-modulus alloys with high strengths by varying the chemistry, or by applying large plastic deformations – e.g. by applying 80% cold working (Niinomi, 2003a). Our goal was to design a net-shape alloy, thus the low-modulus had to be dictated by chemistry alone. For this design purpose, the Bo-Md electronic approach and a model that predicts martensite temperature formation were employed.

2.1.1. Mean d-orbital energy levels and mean bond order

The Bo-Md diagram has been extensively used for the design of titanium alloys (Abdel-Hady et al., 2006). This chart provides useful information about phases and deformation mechanisms as well as elastic modulus of the alloys. The bond order and the metal d-orbital energy level are calculated following:

$$Bo = \sum_i x_i Bo_i \tag{1}$$

$$Md = \sum_i x_i Md_i \tag{2}$$

where x_i is the concentration of element i and Bo_i the i^{th} bonding order value of the element while Md_i the i^{th} d-orbital energy level. Table 1 summarises the Bo and Md values of the elements considered in the present study.

Table 1
Bo and Md values for elements considered in the alloy design process.

Element	Ti	Nb	Ta	Zr	Mo	Sn
Bo	2.79	3.09	3.14	3.08	3.06	2.28
Md	2.44	2.42	2.53	2.93	1.96	2.10

2.1.2. Martensite start temperature (M_s)

This relates to the susceptibility of the alloy to form the martensitic phase, based on (Neelakantan et al., 2009) using the Mo and Al equivalents to include Ta and Sn contributions. The martensitic start temperature (°C) is calculated as a function of the alloy composition following:

$$M_s = 883\text{-}150Fe\ wt.\%\text{-}96Cr\ wt.\%\text{-}49Mo\ wt.\%\text{-}37V\ wt.\%\text{-}17Nb\ wt.\%\text{-}12Ta\ wt.\%\text{-}7Zr\ wt.\%\text{-}3Sn\ wt.\%+15Al\ wt.\% \tag{3}$$

Martensitic start temperature is an indication of the β metastability of the alloy. Our design intent was to obtain a metastable β alloy. This is when BCC β-phase is retained at room temperature from the single-phase field due to the presence of sufficient quantities of β-stabilising elements (Torres-Sánchez et al., 2020) and/or fast cooling rates that inhibit the formation of martensitic (α', α'') or ω-phases when the martensitic start temperature sits within the range 0–200°C (Bignon et al., 2019).

2.2. Strength

Load-bearing alloys must also exhibit good strength. The strength in titanium alloys is controlled by solid-solution strengthening, the phase present, or by the grain size. The grain size is often refined by workability and heat-treatment. However, since we pursue a net-shape manufacturing process, bulk solid-solution strengthening was sought to be the main mechanism used to tailor the strength of this type of alloys. The strength contribution of solid solution strengthening in titanium alloys can be calculated using aluminium and molybdenum equivalents. The following equation (with elemental quantities expressed in wt. %) has been shown as an effective proxy to predict the strength in a variety of titanium chemistries:

$$\sigma = 60[Al]^{\sigma}_{eq.} + 50[Mo]^{\sigma}_{eq.} + 235 \tag{4}$$

Where,

$$[Al]^{\sigma}_{eq.} = Al + \frac{Zr}{3} + \frac{Sn}{6} + 20O + 33N \tag{5}$$

$$[Mo]^{\sigma}_{eq.} = Mo + 1.42Fe + 0.28Nb + 0.22Ta \tag{6}$$

2.3. Biocompatibility (expressed as cell growth)

The effect of chemistry on the biocompatibility of the alloy can be expressed in terms of a coefficient of fibroblastic outgrowth and a relative growth rate of L929 cells. These indices are based in experimentally measured values for individual elements (Kuroda et al., 1998). The relationships can be reported as a function of chemistry following:

$$Bio_1 = 0.8Al + 0V + 1.18Zr + 1.18Nb + 1.17Ta + 0Mo + 0.55Fe + 1.3Sn + 1.57Ti \tag{7}$$

And

$$Bio_2 = 1.2Al + 0V + 1.1Zr + 1.0Nb + 0.9Ta + 1.12Mo + 0Fe + 1.3\,Sn \quad (8)$$

Where the activity was non-dimensionalised to the control (glass = 1.0). Both indices are then combined into a single metric following:

$$Bio = \frac{\frac{Bio_1}{1.57} + \frac{Bio_2}{1.3}}{2} \quad (9)$$

Other factors in addition to mechanical properties and potential for cell growth were also considered in this design process. These were manufacturability and processability of the alloy, quantified in terms of solidification range, a broad quality being associated with risk of hot tearing, and increased susceptibility to chemical heterogeneity during solidification.

2.4. Thermodynamic stability

Elemental partitioning when solidification occurs was simulated using Scheil models (Thermo-Calc, Sweden). This allowed the definition of the envelope of results stemming from variances in local chemistry of the various constituents during solidification as well as changes in density, providing further insight into solid state diffusion of the alloy obtained.

3. Experimental methods

3.1. Materials and manufacturing

Elemental powders (99.5% purity Ti, 99.8% Nb, 99.9% Ta, vacuum dried 99.5% Zr, 99.8% Sn, -325 mesh size, Alfa Aesar, UK; and 99.9% Mo 1–5 μm, Sigma-Aldrich, UK) were used to prepare the alloy by mixing them in an argon atmosphere at the corresponding ratios. Pure Ti samples (labelled c.p.Ti) were prepared and used as control. The mixed powders were made into pellets via cold-isostatic pressing and then vacuum arc remelted (MAM-1 Edmund Bühler, Germany), flipped at least 5 times to achieve homogeneity throughout in an Zr-gettered Ar-atmosphere followed by suction casting into a chilled copper mould to obtain 10 mm diam. 12 mm height cylinders. There was no post processing to the samples.

3.2. Specimen preparation for characterisation

For microscopic characterisation, sections of the cylinders were mounted in epoxy resin of low cure temperature (EpoThin2, Buehler, Germany), ground with P400 grit SiC abrasive paper and polished with 9 μm diamond suspension and 0.02-0.06 μm colloidal silica (Buehler, Germany). For surface morphological observations, 20 vol% H_2O_2 was added to the colloidal silica dispersion in the final step to reveal the microstructures. For surface characterisations (i.e., X-ray photoelectron spectroscopy (XPS) and surface roughness), the sections were ground with P400 and P600 grit SiC paper. The grinding process was performed on all specimens until the same surface roughness was achieved without surface deformation. For the in vitro studies, the discs (1.5 mm thickness and 10 mm diameter sectioned using a IsoMet 15HC blade with a Buehler IsoMet High Speed Pro, Germany) were cleaned as per the procedure reported in (Torres-Sanchez et al., 2017). The samples were sterilised in an autoclave at 121 °C for 1 h and thoroughly rinsed in deionized sterile water.

3.3. Microstructure and surface characterisation methods

Back Scattered Electron (BSE) imaging, Secondary Electron imaging, Energy Dispersive X-ray (EDX) Spectroscopy and Electron Back Scattering Diffraction (EBSD) analyses were performed using a scanning electron microscope (SEM) (JEOL/ZEISS JSM 7800F FESEM, Japan). The X-ray diffraction (XRD) patterns were obtained on a Bruker D2 diffractometer, equipped with Cu Kα radiation (λ = 0.15418 nm), 30 kV of voltage and 10 mA of current. X-ray Photoelectron Spectroscopy (XPS) measurements were carried out on a spectrometer (K-alpha Thermo-Scientific, UK) with an Al source and spectra were curve-resolved (Avantage software with a Shirley-type background function) and charge-corrected to adventitious C 1s spectral component (C–C, C–H) at a binding energy of 284.8 eV. To acquire a depth profile of the oxide composition and chemistry, Ar-ion monomer sputtering was utilised with a low ion energy of 500 eV (to minimise potential artificial chemical reduction of Ti and Nb oxide species) and raster size of 3 mm, yielding a sputter rate of 0.02 nm/s (reference to Ta_2O_5). Roughness measurements were performed using a NPFlex-LA white light interferometer (WLI) (Bruker, USA) to obtain R_a (arithmetic mean deviation of the roughness profile) and R_{Sm} (mean width of the roughness profile) measurements. The electrical state near the surface was measured by means of the surface zeta-potential (ζ) using a Uzgiris dip cell (ZEN 1020) in a Zetasizer Nano ZS system (Malvern Instruments, UK) at room temperature, using the culture media (i.e., α-MEM + 10% FBS + 1% L-glutamine) diluted to 10 vol% with DI water as the electrolyte, and 203 nm diameter polystyrene nanoparticles used as the tracer (3200A Nanosphere Size Standards, Thermo Fisher Scientific, USA). The medium was diluted to lower solution ionic strength below 50 mM to minimise Joule heating and polarisation concentration effects and decrease uncertainty in tracer mobility.

3.4. Thermal and mechanical characterisation

Thermal characterisation of the alloy took place in a differential scanning calorimeter (Shimadzu DSC-60, Japan) using specimens of 40 mg at a heating and cooling rate of 10 °C/min spanning the range from -50 to 200 °C. Compression testing was conducted according to the ASTM E9 standard on samples machined from the as-cast ingots using a lathe to achieve a cylinder of 6 mm diameter and 12 mm height (L/D = 2). Top and bottom faces were ground with P800 grit SiC paper to remove residual rims, burrs and to avoid friction against the UTM platens (T489-73/74) on a 3369 frame fitted with a 50 kN load cell (2530-445) and an external LVDT deflection sensor (2601-062) (Instron, UK). A monotonic load at a constant crosshead displacement ($1.67e^{-2}$ s^{-1}) was applied until plastic deformation was observed. A compliance correction was included in the calculations. The compressive stiffness, i.e., the Young's Modulus, was calculated from the stress-vs-strain gradient and the yield strength was calculated from the departure of linearity in the elastic region.

3.5. In vitro testing and biocompatibility assessment

3.5.1. Cell line and culture media preparation

Culture media was prepared using essential α-MEM enriched with 10% foetal bovine serum FBS (Thermo Fisher Scientific, UK), 1% L-glutamine, and 1% Penicillin-streptomycin (Sigma, UK). Mice pre-osteoblast line MC3T3-E1 at passage 9 were incubated in a 5% CO_2 atmosphere at 37 °C (Thermo Scientific Heracell™ 150, UK). Upon 80% confluency, cells were detached using Trypsin EDTA (0.25% w/v trypsin/0.02% EDTA) (Gibco, Thermo Fisher UK) centrifuged at 150*g for 5 min and seeded (seeding density 1×10^5 cells/well in all cases, except in cell morphology studies) onto the pre-conditioned (i.e., soaked in cell culture media overnight) discs placed in a 24-well low adhesion plate. Media was changed every 2 days for the entire duration of the experiment.

3.5.2. Cell morphology observation and attachment

4 h after seeding 1.2×10^4 cells/well, these were fixed with 4% glutaraldehyde in 0.1 M Cacodylate buffer and refrigerated overnight. Treatment with 2% Osmium Tetroxide (OsO_4) for 2 h at room temperature followed by dehydration (15 min rinsing stages in increasing

Ethanol concentration solution (30%, 50%, 70%, 95% and 100% in triplicate)) and subsequent soaking in three HMDS solutions (2:1 pure ethanol in HMDS, 1:2 pure ethanol in HMDS and final 100% HDMS solution) and left to dry overnight. The discs were mounted and gold/palladium coat-sputtered for cell morphology analysis in SEM.

3.5.3. Cell proliferation, differentiation and early stages of maturation: DNA and protein content quantification. ALP activity

DNA content on the discs was quantified at days 7, 14 and 21 using the PicoGreen® DNA kit (Quanti-iT Picogreen dsDNA, Invitrogen, UK). Samples were washed three times in PBS in order to remove any debris which could interfere with the fluorescent assays. Then, 500 μl of 0.1% Triton-X in deionized water were added to each well and the plate was stored at -80 °C. To achieve complete lysis, the discs were cyclically frozen and thawed at room temperature three times. The cell lysate was collected and stored in 1.5 ml DNAse-free Eppendorfs. 25 μl of each cell/lysis buffer solution were placed into a 96 well plate with 75 μl of dH_2O to a 1:3 dilution. The PicoGreen® solution was prepared as a 1:1200 dilution in 1x Tris-EDTA buffer and 100 μl were added to each sample well. This was stored in darkness for 5 min before fluorescence readings were taken (Ex 480, Em 520 nm).

The osteoinductive properties of the substrates (i.e., their capability to stimulate immature cells to develop into mature osteoblasts) was assessed in a 21-day study. No differentiation supplements were added to the culture media. Alkaline phosphatase (ALP) activity was determined using a 4-Methylumbelliferyl phosphate (4-MUP, Sigma Aldrich, UK) reaction. 50 μl of the cell/lysis buffer solution were placed into the well with 50 μl of dH_2O. Then, 50 μl of 4-MUP were added and left for 30 min. 50 μl of 100 mM EDTA buffer were added to stop the reaction and fluorescence was detected at 360:440 nm (Ex/Em). The total number of proteins was quantified with the 660 nm Pierce Protein assay (Sigma Aldrich, UK) and 10 μl of each lysis solution were transferred to a transparent 96-well microplate. Thereafter, 150 μl of reagent were added to each well and the absorbance was measured at 600 nm (FLUOstar Omega microplate reader, UK). ALP activity and cell protein content were normalised by DNA content and relative number of cells measured on each sample.

3.5.4. Metabolite content

The discs capability to sustain proliferation was evaluated over the 21 days. A 50 μl drop of culture medium was seeded on each disc. After 2 h of incubation at 37 °C, cells adhered onto the material and 1.2 ml of cell culture medium were added to each well. Every second day 1 ml of culture medium was collected and replaced with fresh medium. Media from the samples were stored at -20 °C prior to the measurement of Glucose and L-glutamine concentration (consumption) and its conversion to Lactate and Lactate Dehydrogenase (LDH) (production) (Cedex Bio HT Analyzer, Roche, UK).

3.6. Statistical analysis

Statistical analysis was performed using averages and standard deviation over the results obtained using the repeat specimens or the multiple tests over the same specimen, observing accuracy levels of the

Table 2
Compositional range for alloy design.

Element	Ti	Nb	Ta	Zr	Mo	Sn
Min (wt. %)	50	10	0	0	0	0
Max (wt. %)	90	40	15	15	10	10

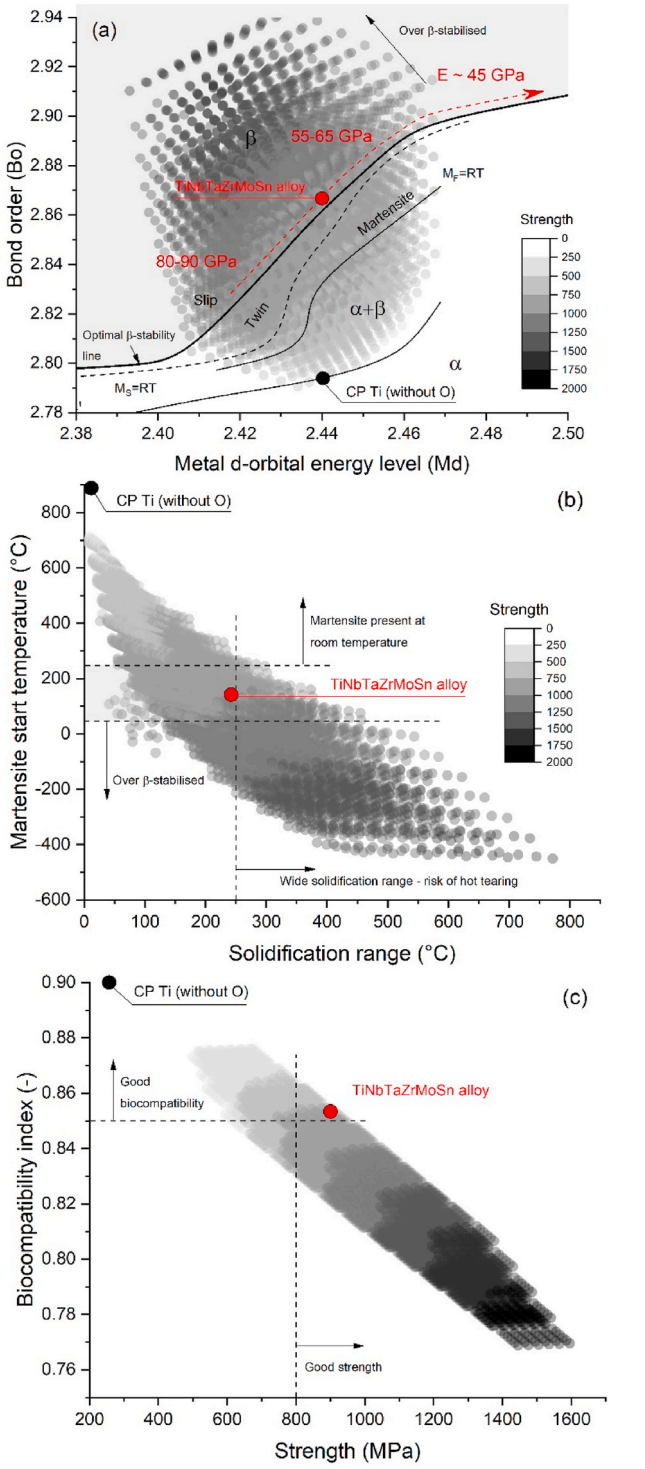

Fig. 1. Alloy design property maps for: (a) Bo-Md diagram, (b) martensite start temperature vs. solidification range, and (c) biocompatibility index vs. strength. Grey dots are the calculated alloys within the compositional space of interest (Table 2), the black dot is c.p.Ti. The red dot represents the properties of the TiNbTaZrMoSn alloy. The colour gradient represents the predictions of a third property (strength). (For interpretation of the references to colour in this figure legend, the reader is referred to the Web version of this article.)

machine and at least in triplicate. Statistical analysis was performed using the computing environment R (R Development Core Team, 2005) and GraphPad Prism (v.7.04). Distribution of data was verified using the Shapiro Normality Test and any significant difference was detected using one-way ANOVA, T-test and Fisher-LSD post-hoc test. Values $p < 0.05$ were considered statistically significant.

4. Results

4.1. Compositional design (modelling), alloy selection and thermodynamic simulation

A large compositional space was explored in the alloy design process. Alloys with varying amounts of Ti, Nb, Ta, Zr, Mo, and Sn were ranged within the minimum and maximum limits of elemental content shown in Table 2.

Fig. 1 shows the predicted property maps for the entire alloy design space defined in Table 2. Fig. 1a shows the calculated Bo-Md maps which displays the empirical correlation between the phase stability of Ti alloys and their modulus of elasticity. This mapping allows a down-selection of the desired alloys since they should sit close to the optimal β-stability line as well as display high Bo-Md values since those have been shown to correlate with lower values of elasticity. Fig. 1b shows the correlation between martensite start temperature and solidification range. The martensite start temperature of the desired alloy falls between room temperature and ~ 200°C with a relatively narrow freezing range (wide freezing ranges are associated with hot tearing and micro segregation). Finally, Fig. 1c shows the trade-off between the calculated biocompatibility index and the predicted strength, i.e., strengths in excess of 800 MPa while maximising the biocompatibility. This multiobjective optimisation led to the designed alloy Ti-27.5Nb-8.5Ta-2.5Zr-3.5Mo-4.5Sn (%wt) (thereafter TiNbTaZrMoSn) indicated with a red dot, which was predicted to possess an optimal balance of the properties above; a strong metastable β-alloy and suitably biocompatible.

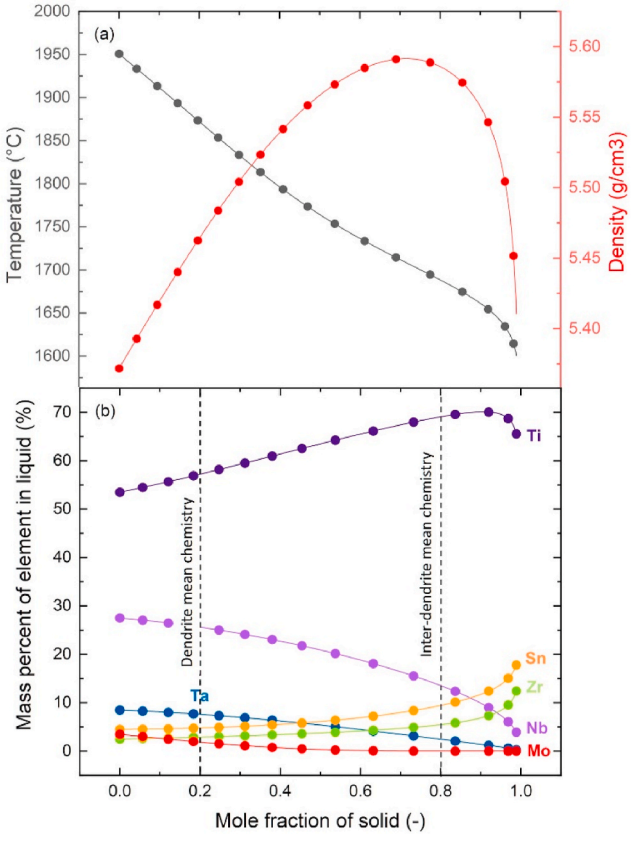

Fig. 2. Predicted solidification behaviour and element partitioning for the TiNbTaZrMoSn alloy: (a) solidification temperature and liquid density vs. mole fraction of solid; (b) mass percentage of each element in liquid vs. mole fraction of solid alloy.

4.2. Thermodynamic simulations

The temperature profile of the solidification process of the melt and its corresponding alloy density variation (Fig. 2a) and diffusion of the liquid phases into the solid, defining intra- and inter-dendritic elemental partitioning boundaries (Fig. 2b), allow an insight into mixture equilibrium. A wide solidification envelope coupled with a wide range of density (Fig. 2a) is associated with large variances in local chemistry during solidification. Fig. 2b quantitatively measures the change in local chemistry as a function of the volume fraction of solidified material under equilibrium conditions. These results predict elemental partitioning when the melt cools, with enrichment of Nb and Ta within the dendrites, which solidify first, and enhanced Ti, Zr and Sn content in the inter-dendritic space that solidifies last.

4.3. Microstructure and phase characterisation of the substrates

The study of the microstructures showed the formation of planar nearly equiaxed grains of different sizes (ave. 141 μm) of fully retained β phase for the TiNbTaZrMoSn alloy (Fig. 3a) and a basket-weave microstructure with α' phase for the c.p. Ti (Fig. 3b). This was confirmed with the XRD analysis results (Fig. 4). Back scattered imaging also revealed dendrite formation in the TiNbTaZrMoSn microstructure throughout the sample due to rapid cooling and solidification compared to the c.p. Ti (Fig. 3c and d). The dendritic growth produced local changes in composition and elemental segregation as confirmed by compositional analysis (Fig. 5a and b). EDX imaging on the ingot mid-section (Fig. 5c) displayed the compositional mapping of the alloy, with partitioning of Nb and Ta into the β dendrites, partitioning of Ti, Sn and Zr into inter-dendritic regions and possible partitioning of Mo towards β dendrites (Table 3). There is however no indication that grain boundaries could have provoked these compositional fluctuations, as it can be seen in Fig. 5b, which shows retained β grains and their respective grain boundaries.

4.4. Surface characterisation: chemical composition, roughness and surface charge

X-Ray Photoelectron Spectroscopy (XPS) was used to investigate the native oxide layer occurring on the substrates in terms of the chemical states of the elemental constituents and in its thickness. Fig. 6 presents the peaks analysed for c.p. Ti (i.e., Ti2p) and TiNbTaZrMoSn (i.e., Ti 2p, Nb 3d5, Ta4d3, Mo3p3, Zr3d, Sn3d) as well as the representation of these data to assess TiO_2 (main constituent) thickness (i.e., when oxygen content diminished by half).

The results indicate that the c.p. Ti has a TiO_2 layer of approx. 4.6 nm in thickness and for TiNbTaZrMoSn this oxide layer is approx. 1.5 nm thick, heavily Nb-doped in which Nb oxidised mainly along with Ti (Table 4). The other oxides present in the layer are Zr oxide, also present throughout the thickness of the Ti oxide, denoting competing oxidation with the Ti and Nb, and Sn oxide, which only spans halfway into that layer. The Ta and Mo oxides content falls below the sensitivity level of the XPS technique (<3%at.).

Surface roughness was measured to confirm that the polishing protocol had derived surfaces of equal roughness parameters, since the study was aimed at assessing discrepancies in the performance of both substrates independent from this variable. The R_a and R_{Sm} for c.p. Ti and TiNbTaZrMoSn alloy are reported in Table 4.

Electrical charge on the substrate surface was measured by means of surface zeta-potential (ζ). Both c.p. Ti and the TiNbTaZrMoSn alloy

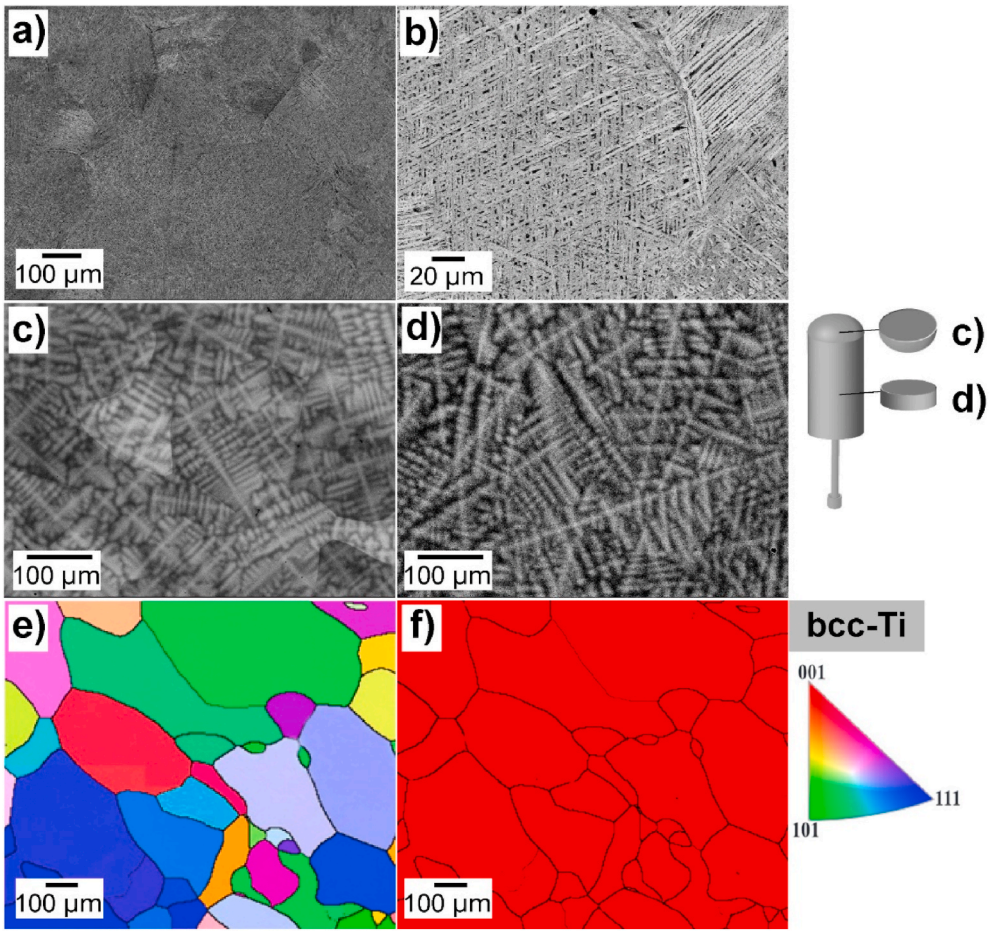

Fig. 3. SEM-BSE imaging of (a) TiNbTaZrMoSn and (b) c.p. Ti. Dendritic solidification was observed on (c) the core and (d) the dome of the alloy cast cylinders. EBSD IPF orientation mapping for (e) TiNbTaZrMoSn, with (f) β grains highlighted along (inset) stereographic triangle for grain orientation on different planes.

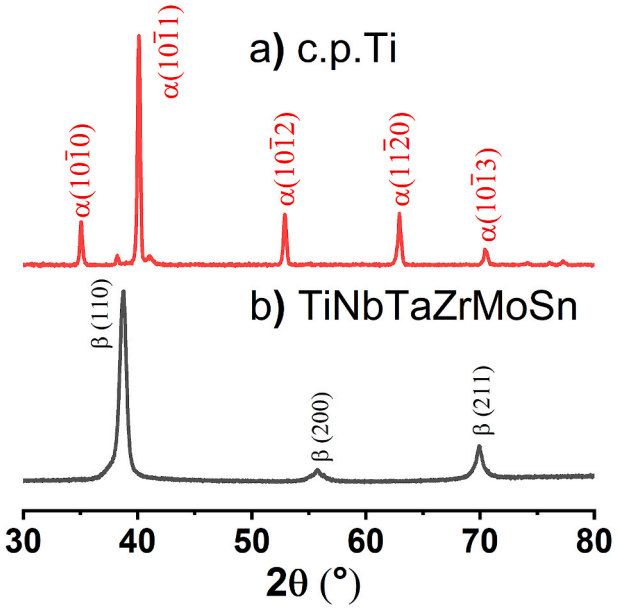

Fig. 4. X-Ray diffraction pattern of (a) c.p. Ti and (b) TiNbTaZrMoSn.

presented a negatively charged surface ζ, with the c.p. Ti being larger in magnitude (Fig. 7). Long term exposure to the culture media increased this magnitude in the c.p. Ti but only slightly in the TiNbTaZrMoSn alloy. There was not a difference after rinsing the samples with DI water, which confirms a long-lasting ionised and functionalised effect on the surfaces. The results from the two substrates in the three different conditions did not present any statistical differences (two-tailed p value $>$ 0.06) (i.e., when comparing c.p. Ti (blank -no soaking-, after 24 h soaking, and after D.I. rinsing) with their counterparts in the alloy). However, there was statistical significance ($p < 0.05$) when comparing the c.p. Ti blank to the two other conditions (i.e., after 24 h soaking and after D.I. rinsing). There was no statistical significance ($p > 0.05$) when comparing the results before and after D.I. rinsing in the c.p. Ti. There were no statistical differences in alloy results, when comparing the alloy blanks, the 24 h soaked and the D.I. rinsed alloy specimens.

4.5. Thermal and mechanical characterisation

The alloy was subjected to a heating and cooling regime to ascertain martensitic transformation start temperature. Fig. 8a depicts the result from a 39.4 mg sample and the heat flow is reported in exothermic and specific units. On heating, a single distinguishable peak at 153 °C is shown. This peak disappeared on a second or third heating/cooling cycle. Upon cooling, the abrupt drop observed after 100 °C also appeared in subsequent heating/cooling cycles. Comparative compressive tests were performed for the c.p. Ti and the TiNbTaZrMoSn alloy (Fig. 8b). The TiNbTaZrMoSn alloy, a fully-retained β phase alloy, presented a lower Young's Modulus than the c.p. Ti. The yield stress was slightly higher for the TiNbTaZrMoSn alloy.

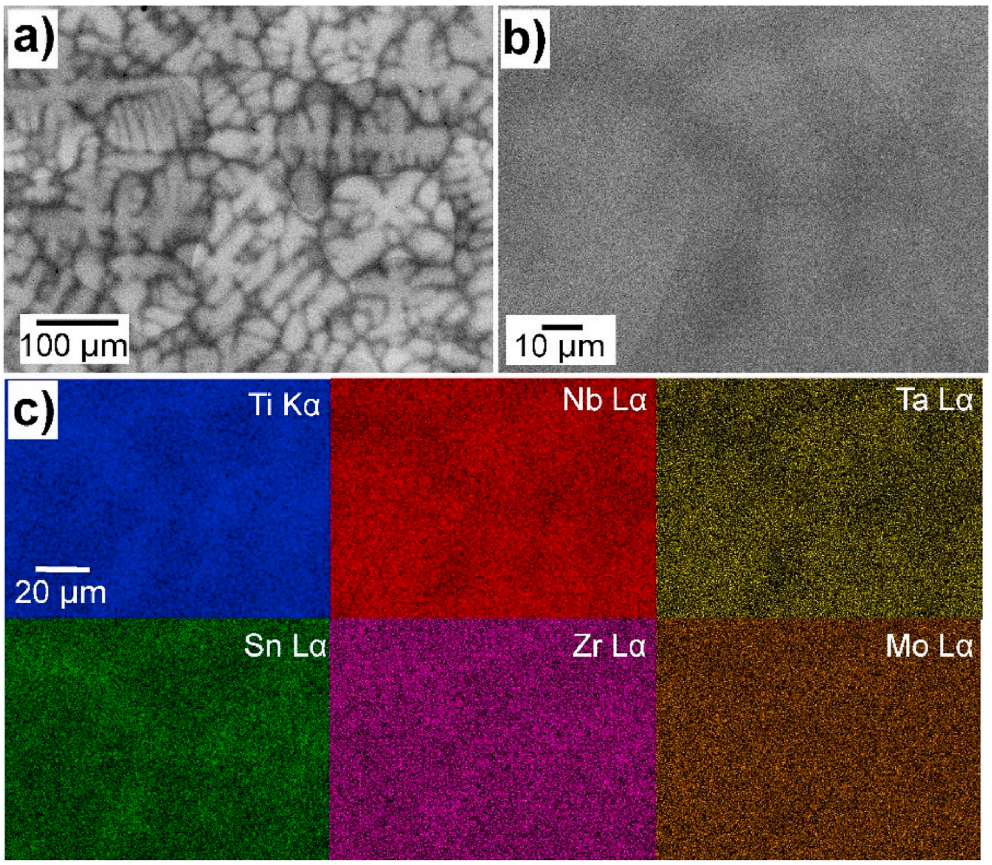

Fig. 5. (a,b) BSE-SEM of TiNbTaZrMoSn, (c) EDX compositional mapping of TiNbTaZrMoSn.

Table 3
Data related to the bulk properties.

Sample ID	Elemental composition (X L-alpha, at.%)						Mechanical (compressive) properties	
	Ti	Nb	Ta	Zr	Mo	Sn	E, GPa	Yield Strength, MPa
c.p.Ti								
	99.5						99.99 ± 2.44	846.61 ± 34.40
TiNbTaZrMoSn							72.61 ± 1.94	945.74 ± 43.14
Area	71.0	19.3	3.1	1.7	1.4	2.5		930.6[a]
Dendrite	68.0	23.1	4.2	1.7	1.5	1.7		995.5[a]
Inter-dendrite	73.4	18.0	2.0	2.2	1.3	3.1		898.0[a]

[a] Predicted values using equations (4)–(6).

4.6. *In vitro testing and biocompatibility assessment*

4.6.1. *Cell morphology, cell proliferation via DNA and protein content quantification, cell metabolism via metabolite content, and cell differentiation via ALP activity*

The imaging results from the early stages of cell attachment (i.e., 4 h after seeding) show cells with multiple tendrils extending in all directions, indicative of good cell attachment to the surface of both substrates (Fig. 9a–d). The EDX analysis results (Fig. 9e and f) show that cells were not attached preferentially to either Ti- nor Nb-enriched areas, since the superposition of the C elemental mapping onto Ti and Nb (Fig. 9e) displays a random distribution of cells on the surface (see Supplementary Fig. S1 for single elemental mappings). The extended pseudopodia morphology indicates non-cytotoxicity of the TiNbTaZrMoSn alloy, also confirmed by the proliferation results (Fig. 10a) and the LDH results.

The study over 21 days provided an insight into cell proliferative rates (in terms of cell numbers), growth rate and size of cells (by means of protein content) and osteogenic properties of the substrates (an indirect measure from Alkaline Phosphatase level (ALP) activity, a mid-late stage marker of cell differentiation) at time points 7, 14 and 21 days (Fig. 10a–c). The values are normalised to cell number to gauge an indication of how cells progress through the different proliferative and differentiation stages into maturation, and to account for any variation in the cell proliferation rate, which is minimal as shown in the cell count study (Fig. 10a). Both c.p. Ti and TiNbTaZrMoSn alloy followed a very similar trend of cell proliferation throughout the 21 days, with the temporary larger rate for the TiNbTaZrMoSn alloy, statistically significant when compared to c.p. Ti at the same time point. Both cell populations stabilised at day 21. Protein content of those cells informed on their volume, and indirectly their growth rate, and the cells incubated onto c.p. Ti were very similar than those on TiNbTaZrMoSn alloy. At day 7 cells incubated on the TiNbTaZrMoSn alloy were statistically significantly larger, but this difference disappeared as the study progressed. The cells volume did not change much between days 7 and 14 but displayed observable growth by day 21. ALP activity level normalised to cell number was markedly lower in the TiNbTaZrMoSn alloy after 14 days into the study, indicating a slower progress toward cell

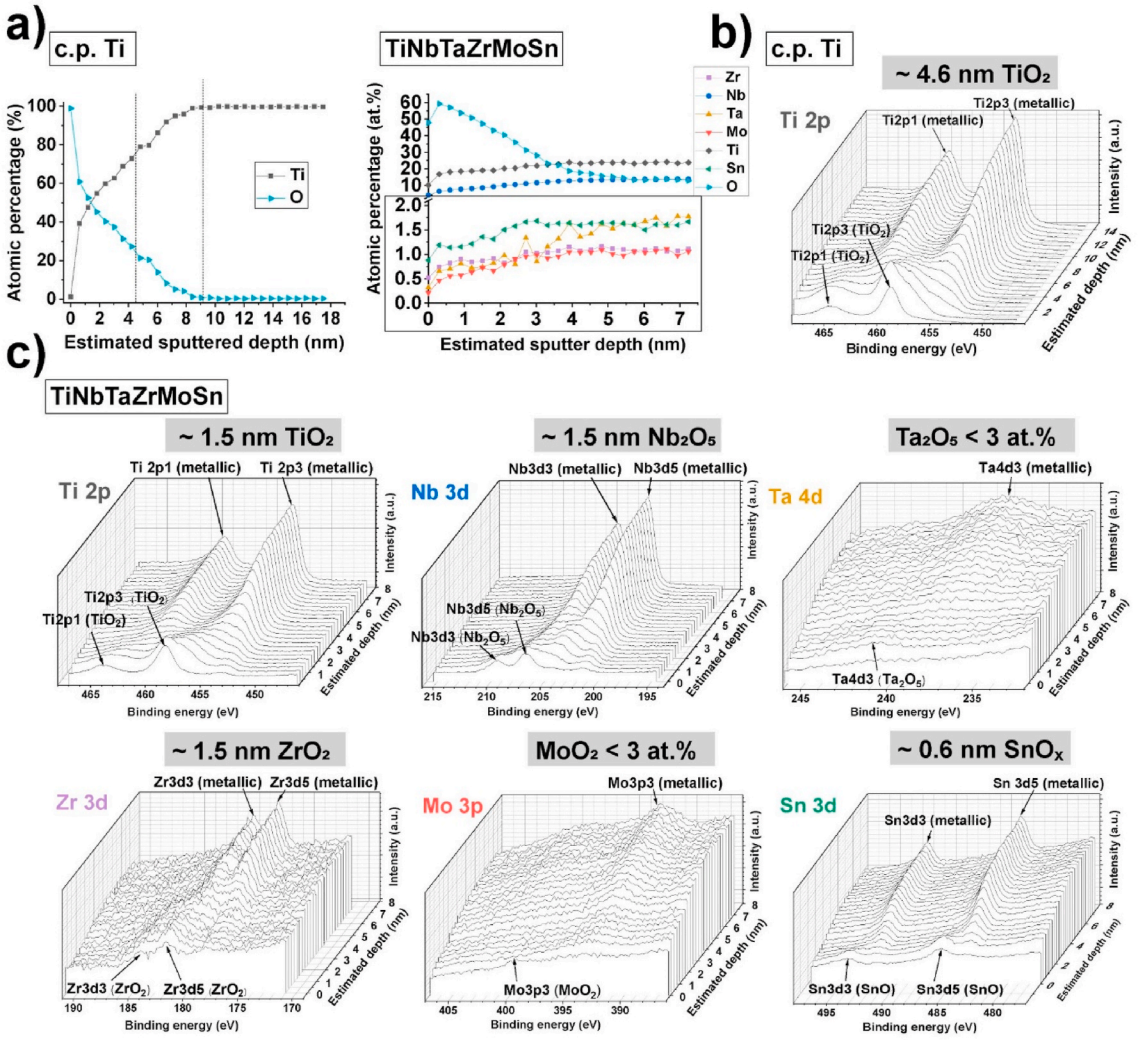

Fig. 6. XPS results for elemental composition (a) c.p. Ti and TiNbTaZrMoSn, and oxide component analysis for (b) c.p. Ti and (c) TiNbTaZrMoSn.

Table 4
Data related to the surface properties.

Sample ID	Oxide in surface, at.%						Oxide thickness, nm	Surface roughness, um	
	TixOx	NbxOx	TaxOx	ZrxOx	MoxOx	SnxOx		R_a	R_{Sm}
c.p.Ti	100.0						4.6	0.293 ± 0.021	33.30 ± 0.20
TiNbTaZrMoSn	63.73	24.63	2.51	2.83	1.77	4.53	1.5	0.310 ± 0.034	39.05 ± 0.75

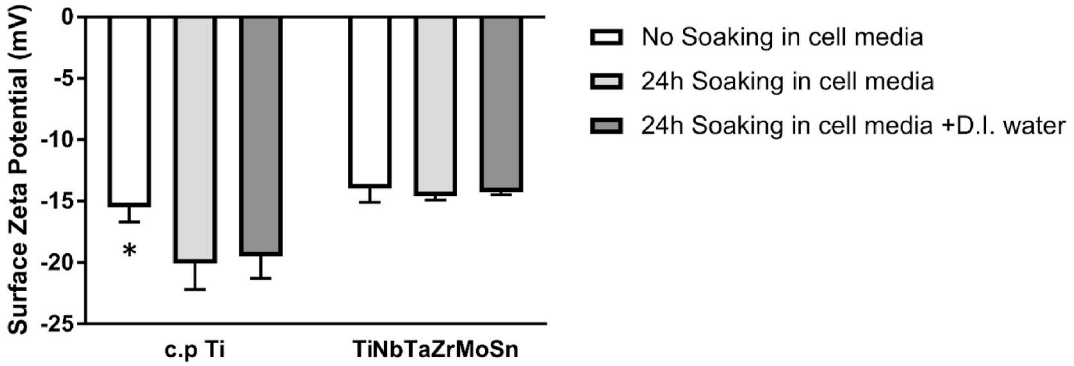

Fig. 7. Surface ζ results from the c.p. Ti and the alloy as a clean surface, after soaking in culture media (mimicking pre-conditioning) and after rinsing with DI water (n = 3) * indicates $p < 0.05$, no marker indicates $p > 0.05$ and no statistical significance.

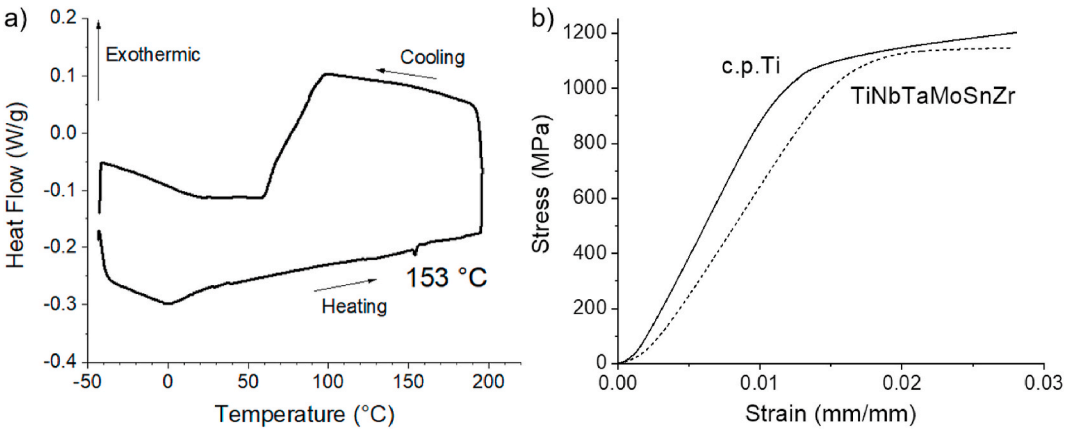

Fig. 8. (a) DSC plot for the alloy, heating and cooling cycles reported as exothermic heat flux; (b) Compressive test results comparative for c.p. Ti and the TiNbTaZrMoSn alloy.

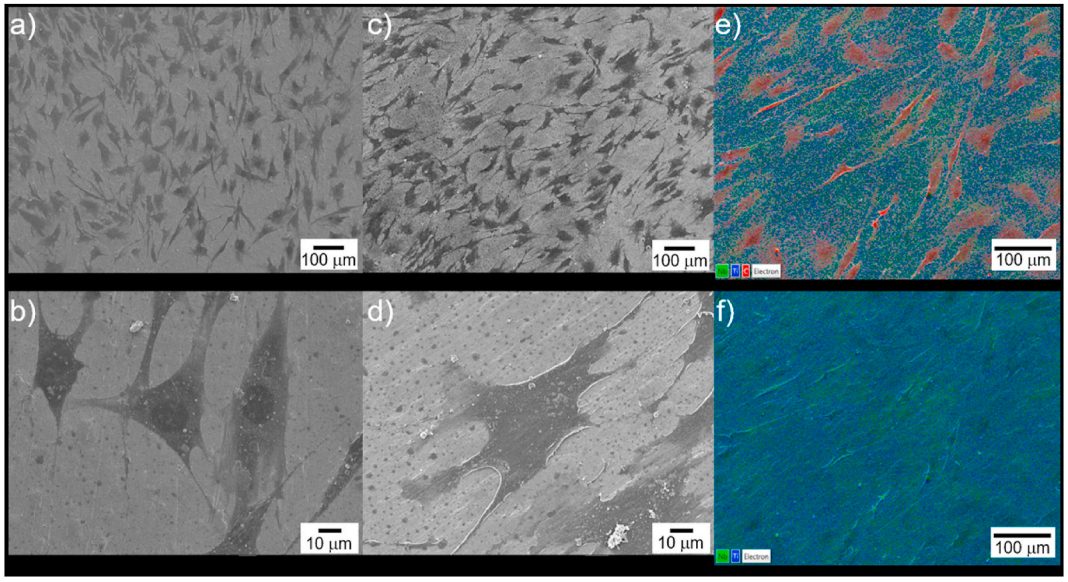

Fig. 9. Cell morphology study after 24 h of attachment using SEM imaging on (a) c.p. Ti and (b) detail, and on (c) TiNbTaZrMoSn alloy, (d) detail; and EDX interrogation of cells on TiNbTaZrMoSn: (e) highlighting C element to locate cells (in red) and (f) Ti (in blue) and Nb (in green) (main constituents of the alloy) in the constituents mapping. The single elemental mappings whose superposition created (e) and (f) can be found in Supplementary S1. (For interpretation of the references to colour in this figure legend, the reader is referred to the Web version of this article.)

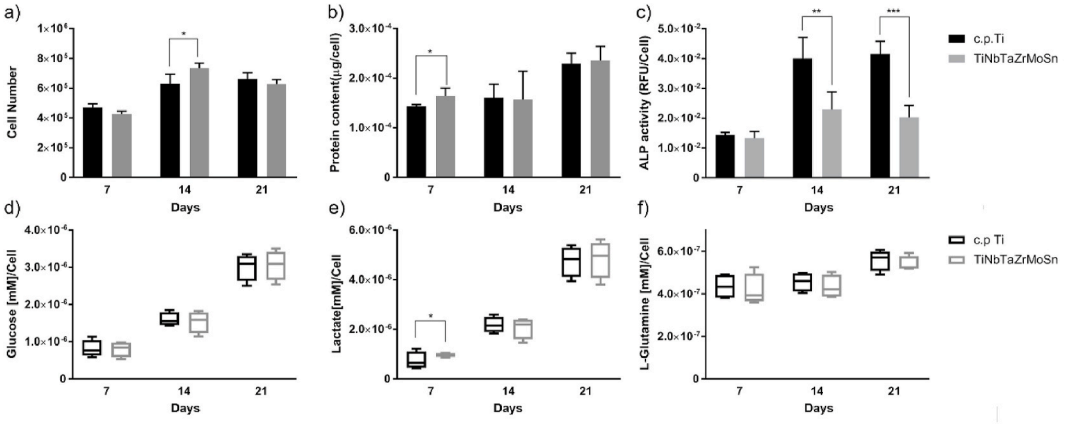

Fig. 10. (a) Cell number (via DNA content), (b) protein content, (c) ALP levels, (d–f) metabolites content evaluated per cell (d) glucose consumption, (e) lactate production, (f) L-glutamine consumption. (n = 4) * indicates $p < 0.05$, **$p < 0.01$, ***$p < 0.001$.

differentiation for the cells incubated onto the alloy compared to those incubated onto c.p. Ti. These results differed with a high degree of statistical significance, as shown in Fig. 10c.

The metabolite activity displayed by the cells throughout the study informed on the metabolic activity of those cells (Fig. 10d–f). The metabolite concentrations are reported to account for cell numbers to include any variation in proliferation. Cells incubated on both c.p. Ti and TiNbTaZrMoSn alloy consumed very similar amounts of glucose as primary energy source (without statistical significance between the substrates) and released similar concentrations of lactate as by-product of the glycolitic pathway (slightly larger at day 7 for TiNbTaZrMoSn alloy showing statistical significance; not the case for days 14 and 21). L-glutamine consumption, supplied to the cells in the cell culture medium and typically a secondary energy resource in the glycolysis pathways for osteoblasts, was slightly lower for the cells incubated on the TiNbTaZrMoSn alloy, albeit without statistical significance, and may be indicative of a preference for glucose as source of energy. No detectable quantities of LDH were observed (below the sensitivity threshold of detection <20 U/ml) over the duration of the experiment on either the cp Ti or the alloy, and therefore are reported as nil.

5. Discussion

Bulk properties of an alloy as well as chemical and physical complexion of a surface play major roles in the successful implantation of medical devices and scaffolds in the host tissue. The mechanical properties (i.e., stiffness and strength), derived from the bulk properties, are responsible for the biomechanical characteristics of the implant in use. The surface properties govern the implant-host tissue interactions from the first instant they come into contact. The surface features mediate cellular adhesion. Cells probe their environment through protein-rich filopodia, attach to the surface to commence a developmental journey modulating cell behaviour through growth, proliferation, differentiation, and maturation, to finally end in mineralisation and consequently bone healing.

In this investigation a β-metastable alloy TiNbTaZrMoSn was selected as a strong contender amongst others with the same alloying constituents because of its predicted manufacturability, and mechanical and biological properties. This led us to believe that the alloy candidate could exhibit an optimal compromise to achieve a biocompatible alloy suitable for orthopaedic applications when manufactured as net-shape and without further post-processing. However, this proposed alloy required ex-silico validation.

5.1. Manufacture, microstructure, elemental composition, thermal, and mechanical properties

Fabricated via vacuum re-melting casting, rapid cooling in the chilled copper mould achieved the formation of a β phase microstructure for TiNbTaZrMoSn retained at RT. The microstructure analysis via BSE, EBSD and XRD confirmed the formation of a β BCC structure (Fig. 3a,e,f; Fig. 4), as expected, albeit presenting dendritic solidification, with local changes in the elemental content when comparing dendrite arms to inter-dendrites (Fig. 3c and d; Fig. 5a). There was chemical elemental composition variation between inter- and dendritic areas (Table 3). The EDX results showed that Nb, Ta and Sn were segregated, with the Nb and Ta enriching the dendrite core and the Sn and Zr accumulated between the dendritic arms. This preferential enrichment of Nb in the dendrite and the Sn between dendrites has been seen in other TiNbSn alloys (Moraes et al., 2014) and it is attributed to the partition coefficients of Nb and Sn dissolved in Ti, which are higher than unity and lower than unity, respectively, as a result of the high melting temperature of Nb. Ta and Zr follow a similar fate to Nb and Sn, being refractory metals as well as transition elements. Nb, Ta and Mo have been reported to enrich dendrites leaving Zr and Sn to accumulate in inter-dendrites in TiNbTaZrMo (Nagase et al., 2018) through segregation due to the miscibility gap of the BCC solid-solution phase. Thermodynamic simulations (Fig. 2) corroborate these experimental results. Simulations predicted a partitioning between Nb/Ta/Mo rich areas and Ti/Zr/Sn rich areas. Incidentally, these areas in the microstructure correspond to dendrites that solidify at the beginning of the process, and inter-dendritic space, which form at the final stages of the solidification process, respectively (Fig. 5, Table 3).

The martensitic start temperature (i.e., a thermal property) measured via DSC did not yield the predicted results (Figs. 1b and 8), which is suspected to be due to the over meta-stabilisation of the alloy or the simplicity of the equation used, that does not consider fully the complexity of this particular alloy. Although small endothermic peaks can be seen upon heating the alloy (Fig. 8a), they do not appear to correspond to significant transformation temperatures, but rather to either the dissolution of small amounts of α' phase crystals, suspected from mechanical tools and handling (e.g. cutting, shearing) or simply thermal ageing from previous stages. These endothermic peaks disappear in the 2nd run, which leads us to conclude that those phases were thermally unstable. We have not detected a martensitic transformation start temperature at the predicted 111 °C by eq. (3). On the contrary, the significant slope-drop upon cooling just below 100 °C persisted in subsequent heating/cooling cycles, which indicates it is a permanent feature of this alloy. It is unclear which thermal transformation takes place at this point, but it is suspected that the diffusion of heavily β-stabilising elements such as Nb, Mo, Ta, Zr, etc. from the β to the α phase could lead to this sustained endothermic flow of heat over a range of temperature as broad as 50 °C.

The mechanical properties, tested via quasi-static uniaxial compression, of the alloy compared to those of c.p. Ti (Table 3, Figs. 1, 8b) demonstrate the lowering of the modulus of elasticity on a par with the predicted results. The TiNbTaZrMo Young's Modulus (72.61 ± 1.94 GPa) is comparable to those of other β metastable alloys reported in literature, though allowing caution in the comparison of alloys created using similar manufacturing processes (i.e., vacuum arc-melting with or without quenching and without post-processing, e.g. heat treatments): Ti–29Nb–13Ta-4.6Zr, 63 GPa (Niinomi, 2003b), Ti-35.5Nb-7.1Zr-5.1Ta, 63 GPa (Elias et al., 2006), Ti–35Nb–10Zr, 65 GPa (Ribeiro et al., 2009), Ti-41.1Nb-7.1Zr, 65 GPa (Elias et al., 2006), and Ti–13Nb–13Zr, 64–77 GPa (Mishra et al., 1996). The value of strength displayed by the c.p. Ti was higher than the one reported (as O free) (Fig. 1). We suspect that our manufactured c.p.Ti possessed a certain amount of oxygen, given the higher chemical affinity of Ti for this element. The strength value for the alloy falls within the values predicted by equations (4)–(6) (Table 3). A lack of published data about this particular alloy prevents direct comparisons, although Ti–12Mo–5Zr which displayed 956 MPa yield strength (Zhao et al., 2011) and as-cast Ti–10Zr–5Nb–5Ta reporting 1010 MPa (Raducanu et al., 2011) could serve as guidance.

Elemental inhomogeneity in the intermediate layer beneath the oxide surface was not expected to influence cell activity, since it had been ascertained already that the cells did not present a preferential attachment location onto the alloys based on localised enrichment of certain elemental constituents (Fig. 9).

5.2. Surface characterisation

Physico-chemical characterisation of the surface properties of the alloy (chemical composition incl. oxide thickness and constituents, roughness, surface ζ) (Table 4, Figs. 6, Figure 7) allowed a comparison with those of the c.p.Ti. The alloy oxide layer was stoichiometrically depleted in Nb, Ta and Mo oxides compared to the elemental constituents, which describes a competing oxidising effect favouring the Ti and Zr elements. The distribution of the alloying elements presented some inhomogeneity (Fig. 5) and this has been reported to lead to the formation of a less stable oxide film (Moraes et al., 2014). The diffusion rate of oxygen through the Ti surface oxide layer decreases with the addition of elements with a valency greater than 4, such as Nb^{5+}, Ta^{5+}, and the

multi-valency $Mo^{4+,5+,6+}$. These M^{5+} can substitute the Ti^{4+} ions in the TiO_2 structure, reducing the amount of anion vacancies (Lütjering et al., 2000). Consequently this had a detrimental effect on the overall oxide layer thickness in the alloy (~1.5 nm), being significantly thinner compared to the c.p.Ti (~4.6 nm).

Because surface roughness plays an important role in cell activity and has been reported as a factor in cell behaviour (i.e., attachment, growth, differentiation (Le Guehennec et al., 2008), this was controlled on all specimens for an appropriate comparison, using roughness values already reported as beneficial for cell attachment and expansion (Anselme et al., 2000; Rosales-Leal et al., 2010) (Table 4). Bone integration affected by surface texture is outwith the remit of this study.

When a surface is implanted in the body, water and electrolytes are the first molecules that the surface (i.e., oxide film, the outermost layer product of the natural re-passivation) will encounter. The characteristics of this layer change due to the formation of an electrokinetic potential (ζ). The surface ζ is the electrical state near the surface and is determined via a laser doppler electrophoresis technique where electro-osmotic flow near the surface is measured through the mobility of a tracer suspended in an electrolyte (Corbett et al., 2012). The surface ζ in this study was measured in culture media, mimicking the conditions the metal surfaces are exposed to during in vitro testing, and therefore provided information on the functional groups at the solid-liquid interface subsequently exposed to the cells. The electrolytic concentration had to be kept very low (10 vol%) to exclude the effect of ionic strength for two reasons: i) to increase signal amplitude; since the potential decreases in magnitude with the increase of electrolyte concentration and the culture medium (i.e., α-MEM) is particularly rich in ions and cations, dilution had to be applied to avoid overloading the sensor; and ii) an increase of electrolyte concentration renders the electrostatic repulsion weaker due to the vicinity of ions, causing a shrinkage of the electrical double layer thickness (Lorenzetti et al., 2016). The results from the surface ζ depict a larger electro-negativity in the c.p. Ti surface immediate surroundings (i.e., more (Lewis) basic sites) due to the hydroxylation (i.e., the OH^- ions product of the dissociation of hydroxyl groups) of the surface immersed in aqueous solution, as well as the attachment of other anions present in the media (e.g. PO_4^{3-}, CO_3^{2-}). On the contrary TiNbTaZrMoSn, although also of negative charge, displayed a smaller absolute value. The presence of T-Nb_2O_5 has been reported to decrease surface ζ at physiological pH compared to TiO_2 (rutile) because of the positively charged (Lewis) acidic sites on the Nb_2O_5 phase given its tetrahedral coordination (Nakajima et al., 2011), instead of the octahedral, which promotes positively charged 'defects' (Jirka et al., 2013). The presence of other minor elements in the alloy such as Sn, the third largest oxide present, also produces a positive shift in surface ζ (Torres-Sanchez et al., 2020). An increase in electrical negativity (in absolute values) occurred after soaking/conditioning in the culture media for the c.p. Ti signifying an enrichment in hydroxyl groups, persistent despite rinsing with D.I. water, but this is not the case for TiNbTaZrMoSn. The adsorption of cations onto the negatively charged surface due to hydroxylation, as well as the attachment of proteins present in the media, appeared to be more prevalent on the c.p. Ti rather than on the alloy.

5.3. Cell activity: attachment, proliferation, and differentiation

It was observed that the cells morphology did not differ between those attached onto c.p.Ti or TiNbTaZrMoSn, and that there were not preferential attachment sites in areas of elemental partitioning enriched by any of the constituents. Filopodia, i.e., thin, protein-rich protrusions that cells use to probe their surrounding environment as well as to reach out to other cells, were visible and well developed (Fig. 9) indicating healthy cells on the substrates. This confirmed non-toxicity and bioactivity of the TiNbTaZrMoSn.

A study on proliferation (reported as cell number), metabolism (via metabolite content), and differentiation (i.e., ALP levels) over 21 days was conducted. Studies on cell numbers (Fig. 10a) indicate that the cells did not display any major difference at days 7 and 21 when comparing the TiNbTaZrMoSn alloy to the c.p. Ti. However, at day 14 there is a statistically significant difference in the larger number of cells incubated on TiNbTaZrMoSn. This time point is significant because it has been reported that this cell line changes phenotype from proliferative to differentiative after day 9 (Quarles et al., 1992). In this case, this suggests that cells incubated onto c.p. Ti are exiting the cell proliferative cycle and entering the differentiation stage at the expected time point, whereas the cells incubated onto TiNbTaZrMoSn alloy are still proliferating and their cell cycle exit delayed. The results from protein content (Fig. 10b) are indicative of cell volume, and with the exception of day 7 when the differences are statistically significant, all cells seem to have similar volumes. Cell numbers and cell volumes results seen simultaneously indicate hypertrophy (i.e., an increase of volume in a cell without cellular proliferation) at day 7 and hyperplasia (i.e., a larger number of cells of equal volume) at day 14. To measure the extent of osteogenic differentiation, ALP activity levels of the cells were measured. ALP activity is an early marker of osteoblast-specific phenotype that is up-regulated during the early phases of osteogenic differentiation. ALP concentrations were normalised to cell numbers to monitor progress into differentiation regardless of the colony size. Greater ALP/cell levels are indicative of greater general cellular population maturity. ALP activity levels of cells incubated on TiNbTaZrMoSn were systematically lower than on c.p. Ti with statistically significant differences at days 14 and 21 (Fig. 10c). Differences between 14 and 21-day timepoints within each of the substrates carried no statistical significance, and while the cells on c.p. Ti upregulated ALP to the same levels at those two timepoints, there is a slight reduction in ALP level at day 21 for the alloy. Although small and within SD range, this drop could be attributed to the slight hyperplasia of cells at that timepoint. Nonetheless, no accelerating effect on cell maturation can be credited to the alloy when compared to c.p. Ti.

The results from the metabolite study indicate the energetic pathway preferred by the cells: the exponential consumption of glucose and the steady concentration of L-glutamine indicate that the cells preferred glucose as the main source of energy to generate ATP (Lee et al., 2017), confirming they followed a glycolytic pathway to meet their energy requirements for proliferation (up to day 14), differentiation (after day 14) and maturation (by day 21) indicated by the resurgence in the consumption of glucose and L-glutamine, and the production of lactate, due to a change in phenotype. However, there is no substantial difference in cell metabolism between the cells incubated on c.p. Ti and on TiNbTaZrMoSn alloy as well as no statistical differences between the cells incubated on the two substrates.

These results indicate that TiNbTaZrMoSn, although non-cytotoxic (indicated by the LDH results) to this cell line, able to sustain good levels of cell attachment and proliferation, and to provide an environment where cells develop a typical metabolic activity, did not upregulate the processes needed to produce ALP for matrix formation as much as c.p. Ti did, and therefore is not inductive of osteogenic development of cells at the same rate as c.p. Ti. These results are contrary to the biocompatibility predictions. Considering the results from sections 4.3 and 4.4, the larger Ti_xO_x content in the thicker oxide layer and more electronegative surface ζ were the reasons behind the better performance of c.p. Ti compared to the TiNbTaZrMoSn alloy. However, the prediction model did not consider these attributes and therefore could not compute them to deliver a fuller and more faithful description of biocompatibility. This aspect, along with the lack of parametric biocompatibility models to assess growth of cells different to fibroblasts (e.g., osteoblasts, pre-osteoblasts or uncommitted cells), cell-cycle exit prediction timings, and differentiation and maturation extents are the main limitations posed in this study that impede a more complete prediction of in silico behaviour and a range of qualities comparable to the set of experimental results obtained.

6. Conclusions

The alloy TiNbTaZrMoSn displayed bulk mechanical properties as predicted by the numerical models, and its metallographic and crystal structure gave it desirable properties for implantable orthopaedic applications (i.e., low modulus of stiffness, high strength). Surface properties studies were carried out independently from roughness and the physico-chemical analysis of the oxide layers delivered a complex picture of competing oxides (Ti, Nb, Zr) along with other elements (Sn, Ta, Mo) and a 3x thinner oxide layer compared to that of the c.p. Ti. The electrical state near the surface in the TiNbTaZrMoSn alloy was less negative (with more positively-charged (Lewis-acidic) sites), even after conditioning with culture media and proteins. In vitro tests revealed that there was no cytotoxic effect from the TiNbTaZrMoSn alloy on the pre-osteoblasts, it promoted cell attachment and proliferation but delayed cell-cycle exit, retarding the start of differentiation when compared to c.p. Ti because TiNbTaZrMoSn did not up-regulate the processes needed to produce ALP that subsequently commences extracellular matrix formation, despite having been predicted otherwise in the models.

The results from this study demonstrate that the extent to which numerical methods can predict bulk properties and microstructure of an alloy is not comparable with the prediction of biological attributes. The latter still falls short and requires further development for a truly in silico design and thereby rapid deployment for customisable and bespoke medical devices.

Author statement

CTS: Conceptualization; Data curation; Formal analysis; Funding acquisition; Methodology; Resources; Validation; Visualization; Writing - original draft; Writing - review & Editing; EA: Conceptualization; Data curation; Formal analysis; Funding acquisition; Software; Visualization; Writing - original draft; review & Editing; JW: materials characterisation: Data curation; Methodology; Visualization; Writing - review & editing; MN: biological testing: Data curation; Methodology; Visualization; Writing - review & editing; PPC: Funding acquisition; Resources; Project administration; Supervision; Validation; Writing - review & editing.

Declaration of competing interest

The authors declare that they have no known competing financial interests or personal relationships that could have appeared to influence the work reported in this paper.

Acknowledgements

Financial support from EPSRC (EP/P027482/1) and Alloyed Ltd is gratefully acknowledged. The Loughborough Materials Characterisation Centre and the Centre for Biological Engineering at Loughborough University have assisted in characterisation tasks. J Singh has supported metrology studies and L Zani sample preparation and running the compression tests. The authors are grateful to Dr M Kaszuba and J Veal, from Malvern Panalytical, for supporting the surface zeta-potential tests.

Appendix A. Supplementary data

Supplementary data to this article can be found online at https://doi.org/10.1016/j.jmbbm.2021.104858.

References

Abdel-Hady, M., Hinoshita, K., Morinaga, M., 2006. General approach to phase stability and elastic properties of β-type ti-alloys using electronic parameters. Scripta Mater. 55 (5), 477–480.

Anselme, K., Linez, P., Bigerelle, M., et al., 2000. The relative influence of the topography and chemistry of tial6v4 surfaces on osteoblastic cell behaviour. Biomaterials 21 (15), 1567–1577.

Bignon, M., Bertrand, E., Tancret, F., et al., 2019. Modelling martensitic transformation in titanium alloys: the influence of temperature and deformation. Materialia 7, 100382.

Corbett, J.C.W., McNeil-Watson, F., Jack, R.O., et al., 2012. Measuring surface zeta potential using phase analysis light scattering in a simple dip cell arrangement. Colloid. Surface. Physicochem. Eng. Aspect. 396, 169–176.

Datta, S., Mahfouf, M., Zhang, Q., et al., 2016. Imprecise knowledge based design and development of titanium alloys for prosthetic applications. J. Mech.Behav.Biomed. Mater. 53, 350–365.

Elias, L.M., Schneider, S.G., Schneider, S., et al., 2006. Microstructural and mechanical characterization of biomedical ti–nb–zr(–ta) alloys. Mater. Sci. Eng., A 432 (1), 108–112.

Guo, Y., Chen, D., Cheng, M., et al., 2013. The bone tissue compatibility of a new ti35nb2ta3zr alloy with a low young's modulus. Int. J. Mol. Med. 31 (3), 689–697.

Gutiérrez Moreno, J.J., Bönisch, M., Panagiotopoulos, N.T., et al., 2017. Ab-initio and experimental study of phase stability of ti-nb alloys. J. Alloys Compd. 696, 481–489.

Huang, L.-F., Grabowski, B., Zhang, J., et al., 2016. From electronic structure to phase diagrams: a bottom-up approach to understand the stability of titanium–transition metal alloys. Acta Mater. 113, 311–319.

Ion, R., Gordin, D.-M., Mitran, V., et al., 2014. In vitro bio-functional performances of the novel superelastic beta-type ti–23nb–0.7ta–2zr–0.5n alloy. Mater. Sci. Eng. C 35, 411–419.

Jirka, I., Vandrovcová, M., Frank, O., et al., 2013. On the role of nb-related sites of an oxidized β-tinb alloy surface in its interaction with osteoblast-like mg-63 cells. Mater. Sci. Eng. C 33 (3), 1636–1645.

Kuroda, D., Niinomi, M., Morinaga, M., et al., 1998. Design and mechanical properties of new β type titanium alloys for implant materials. Mater. Sci. Eng., A 243 (1), 244–249.

Le Guehennec, L., Lopez-Heredia, M.-A., Enkel, B., et al., 2008. Osteoblastic cell behaviour on different titanium implant surfaces. Acta Biomater. 4 (3), 535–543.

Lee, W.-C., Guntur, A.R., Long, F., et al., 2017. Energy metabolism of the osteoblast: implications for osteoporosis. Endocr. Rev. 38 (3), 255–266.

Lorenzetti, M., Gongadze, E., Kulkarni, M., et al., 2016. Electrokinetic properties of tio2 nanotubular surfaces. Nanoscale Research Letters 11 (1), 378.

Lütjering, G., Williams, J.C., Gysler, A., 2000. Microstructure and Mechanical Properties of Titanium Alloys. Microstructure and Properties of Materials 1–77.

Mishra, A.K., Davidson, J.A., Poggie, R.A., et al., 1996. Mechanical and tribological properties and biocompatibility of diffusion hardened ti-13nb-13zr; a new titanium alloy for surgical implants. In: Brown, S., Lemons, J. (Eds.), (Medical Applications of Titanium and its Alloys: the Material and Biological Issues). ASTM International, West Conshohocken, PA.

Moraes, P.E.L., Contieri, R.J., Lopes, E.S.N., et al., 2014. Effects of sn addition on the microstructure, mechanical properties and corrosion behavior of ti–nb–sn alloys. Mater. Char. 96, 273–281.

Morinaga, M., Yukawa, N., Adachi, H., 1986. Electronic structure and phase stability of titanium alloys. Tetsu-To-Hagane 72 (6), 555–562.

Nagase, T., Todai, M., Hori, T., et al., 2018. Microstructure of equiatomic and non-equiatomic ti-nb-ta-zr-mo high-entropy alloys for metallic biomaterials. J. Alloys Compd. 753, 412–421.

Nakajima, K., Baba, Y., Noma, R., et al., 2011. Nb2o5·nh2o as a heterogeneous catalyst with water-tolerant lewis acid sites. J. Am. Chem. Soc. 133 (12), 4224–4227.

Neacsu, P., Gordin, D.-M., Mitran, V., et al., 2015. In vitro performance assessment of new beta ti–mo–nb alloy compositions. Mater. Sci. Eng. C 47, 105–113.

Neelakantan, S., Rivera-Díaz-del-Castillo, P.E.J., van der Zwaag, S., 2009. Prediction of the martensite start temperature for β titanium alloys as a function of composition. Scripta Mater. 60 (8), 611–614.

Niinomi, M., 2003a. Recent research and development in titanium alloys for biomedical applications and healthcare goods. Sci. Technol. Adv. Mater. 4 (5), 445–454.

Niinomi, M., 2003b. Fatigue performance and cyto-toxicity of low rigidity titanium alloy, ti–29nb–13ta–4. 6zr. Biomaterials 24 (16), 2673–2683.

Noori Banu, P.S., Devaki Rani, S., 2018. Artificial neural network based optimization of prerequisite properties for the design of biocompatible titanium alloys. Comput. Mater. Sci. 149, 259–266.

Quarles, L.D., Yohay, D.A., Lever, L.W., et al., 1992. Distinct proliferative and differentiated stages of murine mc3t3-e1 cells in culture: an in vitro model of osteoblast development. J. Bone Miner. Res. : the Off. J.Am. Soc.Bone Miner. Res. 7 (6), 683–692.

Raabe, D., Sander, B., Friák, M., et al., 2007. Theory-guided bottom-up design of β-titanium alloys as biomaterials based on first principles calculations: theory and experiments. Acta Mater. 55 (13), 4475–4487.

Raducanu, D., Vasilescu, E., Cojocaru, V.D., et al., 2011. Mechanical and corrosion resistance of a new nanostructured ti–zr–ta–nb alloy. J. Mech.Behav.Biomed. Mater. 4 (7), 1421–1430.

Ribeiro, A.L.R., Junior, R.C., Cardoso, F.F., et al., 2009. Mechanical, physical, and chemical characterization of ti–35nb–5zr and ti–35nb–10zr casting alloys. J. Mater. Sci. Mater. Med. 20 (8), 1629–1636.

Rosales-Leal, J.I., Rodríguez-Valverde, M.A., Mazzaglia, G., et al., 2010. Effect of roughness, wettability and morphology of engineered titanium surfaces on osteoblast-like cell adhesion. Colloid. Surface. Physicochem. Eng. Aspect. 365 (1), 222–229.

Song, Y.-H., Kim, M.-K., Park, E.-J., et al., 2014. Cytotoxicity of alloying elements and experimental titanium alloys by wst-1 and agar overlay tests. Dent. Mater. 30 (9), 977–983.

Sultana, N., Sikdar, S., Chattopadhyay, P.P., et al., 2014. Informatics based design of prosthetic ti alloys. Mater. Technol. 29 (Suppl. 1), B69–B75.
Torres-Sanchez, C., Al Mushref, F.R.A., Norrito, M., et al., 2017. The effect of pore size and porosity on mechanical properties and biological response of porous titanium scaffolds. Mater. Sci. Eng. C 77, 219–228.
Torres-Sanchez, C., Norrito, M., Wang, J., et al., 2020. Physico-chemical characterisation of ti-nb-sn alloys surfaces and their osteogenic properties. Surf. Coating. Technol. 403, 126439.
Torres-Sánchez, C., Wang, J., Norrito, M., et al., 2020. Addition of sn to tinb alloys to improve mechanical performance and surface properties conducive to enhanced cell activity. Mater. Sci. Eng. C 115, 110839.
Zhang, L.-C., Chen, L.-Y., 2019. A review on biomedical titanium alloys: recent progress and prospect. Adv. Eng. Mater. 21 (4), 1801215.
Zhao, C., Zhang, X., Cao, P., 2011. Mechanical and electrochemical characterization of ti–12mo–5zr alloy for biomedical application. J. Alloys Compd. 509 (32), 8235–8238.